Editors' Suggestion

Fast computation of Wigner functions of undulator radiation in a multiple-beam-waist configuration

Takashi Tanaka*

RIKEN SPring-8 Center, Koto 1-1-1, Sayo, Hyogo 679-5148, Japan

(Received 28 January 2026; accepted 4 September 2026; published 10 November 2026)

In the formulation of synchrotron radiation (SR), the Wigner function represents the photon flux density in the four-dimensional phase space, and thus defines the brilliance and coherence. Although we have to rely on a numerical method to evaluate the Wigner function for a realistic electron beam, a convolution approach is available under the assumption that each electron travels along a straight line apart from a sinusoidal motion driven by an undulator magnetic field. As a result, the computation of Wigner functions for typical SR sources is usually completed within an acceptable time. It should be noted, however, that the above assumption is violated in a multiple-beam-waist (MBW) configuration, in which the lattice function is designed to have more than one beam waist position where the vertical betatron function is optimized to accommodate a narrow-gap undulator. In such a case, we have to carry out a Monte Carlo simulation, which requires a huge amount of time to get a reliable result. To overcome this difficulty, we introduce a theoretical-numerical method aimed at reducing the cost of computing Wigner functions in the MBW configuration. We show that the computation time can be saved by 2–4 orders of magnitude by means of the proposed method.

DOI: 10.1103/4hnq-5t8d

I. INTRODUCTION

The Wigner function, which was originally introduced to describe the probability function of a quantum state [1], has been widely used in the formulation of synchrotron radiation (SR), or more specifically, undulator radiation (UR) [2–7]. Mathematically, it represents the photon flux density in the four-dimensional (4D) transverse phase space, and thus is related to the performance of UR as a light source, such as the brilliance and coherence. Furthermore, the Wigner function can be applied to the propagation of partially coherent UR by means of a coherent mode decomposition method [8].

As is the case with other properties, the Wigner function of UR emitted by a realistic electron beam cannot be calculated analytically, and we have to carry out a fivefold integral to take into account the effects due to the finite emittance and energy spread of the electron beam. Even so, computation of the Wigner function for typical undulators is usually completed within a reasonable time, because the fourfold integral relevant to the finite emittance can be done rather quickly with the assistance of the convolution and fast Fourier transform algorithms [7].

In the above discussion concerning the computation of the Wigner function of UR, one important assumption is made: the undulator is located in a magnet-free section or in a drift space without any focusing magnets. As a result, each electron travels along a straight line, apart from a sinusoidal motion driven by the magnetic field of the undulator. Although this assumption is valid in most undulator configurations, we have two possibilities to violate it.

One is the so-called undulator natural focusing, in which electrons are focused in the direction of the undulator magnetic field. In the case of a conventional planar undulator generating a vertical magnetic field, an electron injected with a vertical offset is gradually deflected in the same direction because of this effect. Note that, however, the focusing strength is inversely proportional to the square of the electron energy, and thus this effect can be neglected in typical SR facilities operated with an electron energy higher than a few GeV.

The other is a segmented undulator combined with additional focusing magnets; in this configuration, the lattice function in the straight section is designed to have more than one beam waist position where the vertical betatron function is optimized to accommodate a narrow-gap undulator. Obviously, the "magnet-free" assumption is violated in such a "multiple-beam-waist" (MBW) configuration, and thus the computation of the Wigner function, or the fivefold integral, should be carried out by a

*Contact author: ztanaka@spring8.or.jp

Published by the American Physical Society under the terms of the Creative Commons Attribution 4.0 International license. Further distribution of this work must maintain attribution to the author(s) and the published article's title, journal citation, and DOI.

Monte Carlo simulation. As easily understood, the computation time to get a reliable result largely depends on the electron beam emittance and the wavelength of UR.

An example of the MBW configuration is found in BL43LXU of SPring-8 [9], where three undulator segments are installed together with two sets of quadrupole triplets in between to provide bright x-ray beams between 14.4 and 26 keV. Because the horizontal emittance in SPring-8 is relatively larger than the diffraction-limited emittance in this energy range, the computation of the Wigner function takes a huge amount of time; as presented later, the computation time is about several orders of magnitude longer than what is needed when the magnet-free assumption is applicable. This makes the application of the Wigner function less feasible in the MBW configuration, and thus an alternative solution that is more numerically efficient is demanded, which is the main scope of this paper.

II. WIGNER FUNCTION IN THE MBW CONFIGURATION

A. Accelerator layout

Before discussing the Wigner function in the MBW configuration, let us define the layout of the focusing magnets and undulator segments, together with the coordinate system to be used throughout this paper. Figure 1 shows the layout in the case of three segments, where three undulators (green) and two sets of quadrupole triplets (red/cyan) are installed in the same straight section; L and L_u denote the intersegment distance and undulator length, while L_M is the length of the matching section accommodating the quadrupole triplet. Note that we apply a thin-lens approximation to simplify the transfer matrix. Figure 1 also defines the coordinate system for mathematical operations in the following discussions, where x, y, and z form a Cartesian coordinate system, with z denoting the longitudinal axis.

We assume that the whole straight section is divided into a number of subsections, within which the trajectory of each electron is defined by a straight line. In other words, each subsection can be regarded as a magnet-free section. Then the subsection boundaries coincide with the focusing magnet positions as indicated by z_l, where l is an integer specifying the index of subsection. By definition, z_0 is located at the origin, or the center of the straight section ($z_0 = 0$) as shown in the figure, and the lth subsection is defined by $z_l \le z \le z_{l+1}$. An electron injected with an offset in position and/or angle is kicked by the focusing magnets at the subsection boundaries; in other words, the electron undergoes betatron oscillation besides the sinusoidal motion in the undulator as indicated by the blue solid line.

B. Wigner function by a single electron undergoing betatron oscillation

Now let us consider the Wigner function of UR emitted by a single electron undergoing betatron oscillation. We start from the angular representation of the complex amplitude of radiation (electric field in the frequency domain) at a fixed wavelength of λ, which is given as [4,7],

$$\mathcal{E}(\boldsymbol{\theta}) = \int [\beta_x(z) - \theta_x] \mathrm{e}^{i\Phi(z)} dz, \tag{1}$$

with

$$\Phi(z) = \frac{k}{2}\left[\left(\frac{1}{\gamma^2} + \theta^2\right) z + \int_0^z \boldsymbol{\beta}^2(z')dz' - 2\boldsymbol{\theta}\cdot\boldsymbol{r}_e(z)\right], \tag{2}$$

where $\boldsymbol{r}_e \equiv (x_e, y_e)$, $\boldsymbol{\beta} \equiv (\beta_x, \beta_y)$, and γ denote the transverse position, relative velocity, and Lorentz factor of the electron, $\boldsymbol{\theta} \equiv (\theta_x, \theta_y)$ denotes the angular coordinate, and $k = 2\pi/\lambda$ is the wave number of radiation. Mathematically, $\mathcal{E}$ is defined as the spatial and temporal Fourier transform of the electric field of radiation, virtually observed at the origin. Note that horizontally-polarized radiation is supposed in the above formula (1), although extending to a more general polarization state is straightforward. In addition, the unit-conversion coefficient is omitted for simplicity.

Next, we define a local complex amplitude at the ith undulator segment,

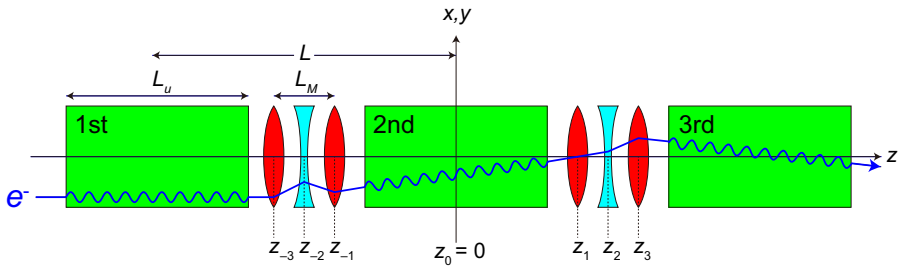


FIG. 1. Layout of undulators (green) and focusing magnets (red and cyan) in the MBW configuration in the case of three segments.

$$\mathcal{E}_i(\boldsymbol{\theta}) = \int_{Z_{u,i}}^{Z_{d,i}} [\beta_x(z) - \theta_x] \mathrm{e}^{i\Phi(z)} dz, \tag{3}$$

where $Z_{u,i}$ and $Z_{d,i}$ mean the upstream and downstream ends of the ith undulator segment. Neglecting the radiation generated at the focusing magnets, we have

$$\mathcal{E} = \sum_{i=1}^{N_u} \mathcal{E}_i, \tag{4}$$

with N_u being the number of undulator segments. Because no focusing magnets are present between the subsection boundaries, the trajectory of an electron in the ith undulator segment is given by

$$\boldsymbol{\beta}(z) = \langle \boldsymbol{\beta} \rangle(z) + \tilde{\boldsymbol{\beta}}_i, \quad \boldsymbol{r}_e(z) = \langle \boldsymbol{r} \rangle(z) + \tilde{\boldsymbol{r}}_i + \tilde{\boldsymbol{\beta}}_i z, \tag{5}$$

where $\langle \boldsymbol{\beta} \rangle$ and $\langle \boldsymbol{r} \rangle$ describe the motion of a reference electron traveling along the undulator axis, $\tilde{\boldsymbol{\beta}}_i$ and $\tilde{\boldsymbol{r}}_i$ define the angular and positional offsets in the ith undulator. It should be noted that $\tilde{\boldsymbol{r}}_i$ is given by extending the trajectory in the ith undulator straight to the origin of z, as illustrated in Fig. 2. This should be distinguished from the real offset at the origin ($\boldsymbol{r}_0$), because the electron is kicked by the focusing magnets at the subsection boundaries.

Substituting Eq. (5) into (2) and (3), we have

$$\mathcal{E}_i(\boldsymbol{\theta}) = \int_{Z_{u,i}}^{Z_{d,i}} [\langle \beta \rangle_x(z) - (\theta_x - \tilde{\beta}_{xi})] \mathrm{e}^{i\Phi(z)} dz, \tag{6}$$

with

$$\Phi(z) = \frac{k}{2} \left\{ \left[\frac{1}{\gamma^2} + (\boldsymbol{\theta} - \tilde{\boldsymbol{\beta}}_i)^2 \right] z + \int_0^z \langle \boldsymbol{\beta} \rangle^2(z') dz' - 2(\boldsymbol{\theta} - \tilde{\boldsymbol{\beta}}_i) \cdot \langle \boldsymbol{r} \rangle(z) - 2\tilde{\boldsymbol{r}}_i \cdot \boldsymbol{\theta} \right\} + \phi_i, \tag{7}$$

where ϕ_i is the phase term coming from the temporal delay due to the betatron oscillation and is given as

$$\phi_i = \frac{k}{2} \begin{cases} \sum_{l=0}^{L(i)-1} (z_{l+1} - z_l)(\boldsymbol{\beta}_l^2 - \tilde{\boldsymbol{\beta}}_i^2) & ; Z_{u,i} > 0, \\ \sum_{l=L(i)+1}^{-1} (z_l - z_{l+1})(\boldsymbol{\beta}_l^2 - \tilde{\boldsymbol{\beta}}_i^2) & ; Z_{d,i} < 0, \\ 0 & ; Z_{u,i} \le 0 \le Z_{d,i}, \end{cases} \tag{8}$$

where $L(i)$ means the index of the subsection that contains the ith undulator segment as shown in Fig. 2, and $\boldsymbol{\beta}_l$ means the angular offset at the lth subsection. It should be noted that $\tilde{\boldsymbol{\beta}}_i$ and $\boldsymbol{\beta}_i$ are different, because the former is numbered by the undulator segment, while the latter is by the subsection; to be more specific, $\tilde{\boldsymbol{\beta}}_i = \boldsymbol{\beta}_{L(i)}$.

Let us now define a reference complex amplitude $\bar{\mathcal{E}}_i$, which corresponds to the radiation emitted by the reference electron at the ith undulator and is given by substituting $\tilde{\boldsymbol{r}}_i = \tilde{\boldsymbol{\beta}}_i = \boldsymbol{0}$ into Eq. (6) and so on. Then we have an important formula

$$\mathcal{E}_i(\boldsymbol{\theta}) = \bar{\mathcal{E}}_i(\boldsymbol{\theta} - \tilde{\boldsymbol{\beta}}_i) \exp(i\phi_i) \exp(-ik\tilde{\boldsymbol{r}}_i \cdot \boldsymbol{\theta}), \tag{9}$$

which is similar to what has been derived in a former paper [4], except for the phase term ϕ_i coming from the betatron oscillation.

The Wigner function of UR emitted by a single electron undergoing the betatron oscillation is given by substituting Eqs. (3) and (4) into

$$W(\boldsymbol{r}, \boldsymbol{\theta}) = \frac{k^2}{4\pi^2} \int d\boldsymbol{\theta}' \mathrm{e}^{-ik\boldsymbol{\theta}' \cdot \boldsymbol{r}} \Gamma(\boldsymbol{\theta}, \boldsymbol{\theta}'), \tag{10}$$

with

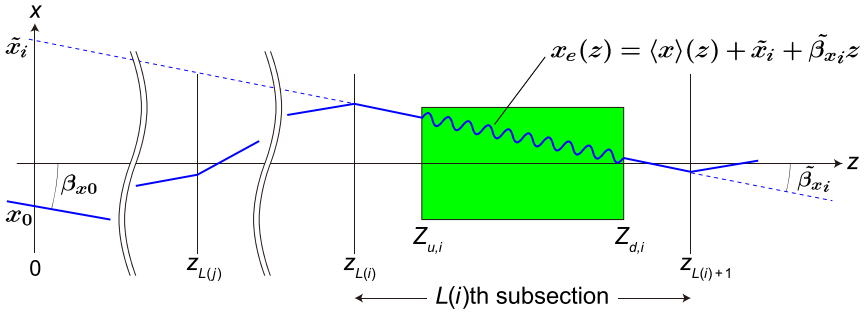


FIG. 2. Trajectory of an electron in the horizontal direction, which has positional and angular offsets $\tilde{x}_i$ and $\tilde{\beta}_{xi}$ at the ith undulator segment located downstream of the origin ($Z_{u,i} > 0$).

$$\Gamma(\boldsymbol{\theta},\boldsymbol{\theta}') = \mathcal{E}^*\left(\boldsymbol{\theta}+\frac{\boldsymbol{\theta}'}{2}\right)\mathcal{E}\left(\boldsymbol{\theta}-\frac{\boldsymbol{\theta}'}{2}\right), \tag{11}$$

where $\boldsymbol{r} \equiv (x, y)$ denotes the spatial coordinate. Note that Γ is known as the cross spectral density (CSD), and the Wigner function is defined as the Fourier transform of the CSD.

As mentioned earlier, $W(\boldsymbol{r},\boldsymbol{\theta})$ represents the photon flux density in the 4D phase space spanned by $\boldsymbol{r}$ and $\boldsymbol{\theta}$. For later discussions, we define 2D (horizontally and vertically projected) Wigner functions as follows

$$W_x(x,\theta_x) = \int\int W(\boldsymbol{r},\boldsymbol{\theta})dyd\theta_y,$$
$$W_y(y,\theta_y) = \int\int W(\boldsymbol{r},\boldsymbol{\theta})dxd\theta_x, \tag{12}$$

which denote the photon flux density in the 2D phase spaces. In addition, we define the brilliance as the on-axis Wigner function as follows

$$\mathcal{B} = W(\mathbf{0},\mathbf{0}), \qquad \mathcal{B}_x = W_x(0,0), \qquad \mathcal{B}_y = W_y(0,0). \tag{13}$$

C. Wigner functions evaluated by Monte Carlo simulations

Having derived the formulas to evaluate the Wigner function of UR emitted by a single electron undergoing the betatron oscillation in the MBW configuration, let us consider the method of how to compute the Wigner function for a realistic electron beam with the finite emittance and energy spread. Obviously, the most straightforward way is the Monte Carlo simulation explained as follows.

First, a large number (N_p) of particles are generated, whose energy and injection condition (angle and position) are determined by the distribution function of the electron beam. Next, trajectory offsets at the ith undulator segment ($\tilde{\boldsymbol{\beta}}_i$ and $\tilde{\boldsymbol{r}}_i$) and the angular offset at the lth subsection ($\boldsymbol{\beta}_l$) are evaluated to compute the complex amplitude $\mathcal{E}$ and Wigner function W for individual particles, using Eqs. (4), (9), and (10). The results are then averaged over the N_p particles to represent the Wigner function evaluated with them. In the above numerical process, the computation of the reference complex amplitude $\bar{\mathcal{E}}_i$ does not have to be repeated for each particle, and can be done in advance.

As an example, we carried out the Monte Carlo simulation described above to evaluate the Wigner functions in the MBW configuration, assuming the parameters in the SPring-8 BL43LXU summarized in Table I. Although up to three undulator segments are available in this beamline, we selected two segments to simplify the problem and save the computation time.

TABLE I. Electron and undulator parameters in SPring-8 BL43LXU.

Electron energy	8 GeV
Beam current	100 mA
Natural emittance	2.4×10^{-9} m rad
Coupling constant	0.002
Energy spread	1.1×10^{-3}
Horizontal betatron function	18 m
Vertical betatron function	2.5 m
Undulator period	19 mm
Undulator K value	1.43
Fundamental photon energy	15.8 keV
Segment length (L_u)	5 m
Intersegment distance (L)	10.7 m
Matching section length (L_M)	4.5 m

To investigate the numerical convergence, we repeated the simulation for different numbers of particles $N_p = 10^3 \times 2^m$, where m denotes an integer to specify the cycle of simulation. We also carried out the simulations with and without the effect of the energy spread of the electron beam to investigate its impact. Figures 3(a)–3(e) show the horizontally projected Wigner functions (W_x) computed at $101(x) \times 81(\theta_x)$ grid points for different numbers of cycles ($2 \le m \le 6$), in which the energy spread is neglected.

As found from the simulation results, we need a large number of particles to suppress the numerical artifacts and get a reliable result; this is attributable to that the horizontal emittance of the electron beam is much larger than the diffraction-limited emittance at 15.8 keV. To quantify the number of particles to reach the numerical convergence, let us define a numerical error as the maximum difference from the former cycle, normalized by the maximum value; to be specific, it is defined as

$$\epsilon(m) = \frac{\max[|W_{m,x}(x,\theta_x) - W_{m-1,x}(x,\theta_x)|]}{\max[W_{m,x}(x,\theta_x)]}, \tag{14}$$

where $W_{m,x}(x,\theta_x)$ is the projected Wigner function computed with $N_p = 10^3 \times 2^m$ particles. The numerical error evaluated for each value of N_p is indicated in Fig. 3, where we find that more than 32,000 particles are needed to reduce the numerical error below 10%. In addition, the characteristic fringe pattern near the axis ($x = 0$) cannot be well identified if N_p is less than 32,000.

Although the fringe pattern mentioned above is specific to the MBW configuration in the electron beam condition currently under discussion, it does not actually survive in a realistic electron beam as shown in Fig. 3(f), where the simulation was carried out using the same parameters as those in Fig. 3(e), but with the energy spread taken into account. We find that the central fringe pattern completely disappears; in other words, the energy spread works to

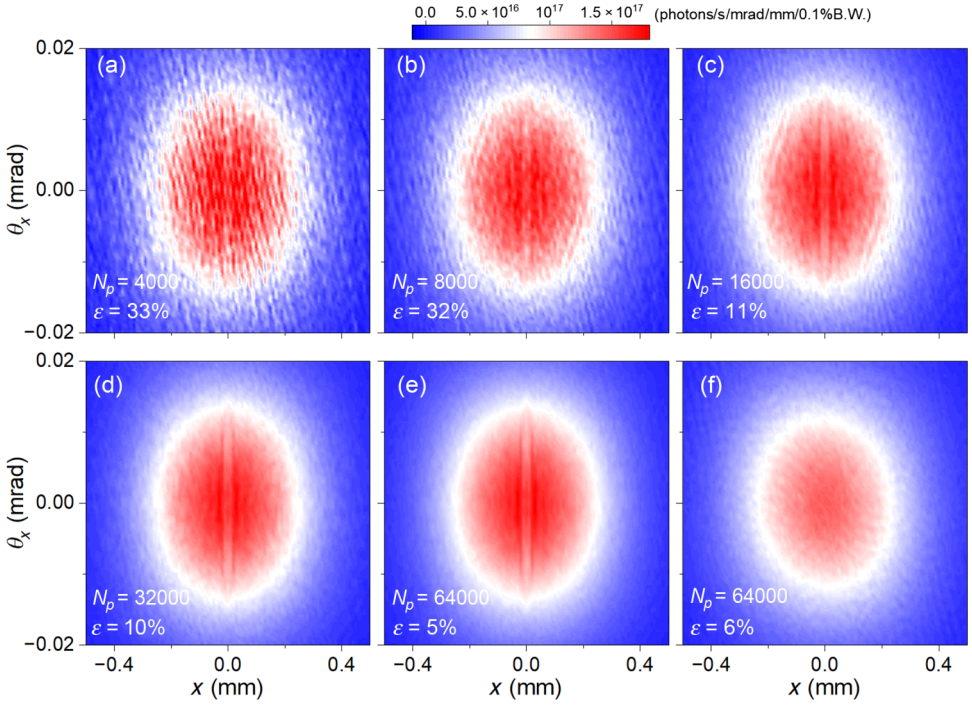


FIG. 3. Horizontally projected Wigner functions evaluated by the Monte Carlo simulation with different numbers of particles. Note that the energy spread of the electron beam is neglected in (a)–(e) but taken into account in (f).

wash out the characteristic pattern coming from the MBW configuration.

Figures 4(a) and 4(b) show the vertically projected Wigner function (W_y) computed at $51(y) \times 51(\theta_y)$ grid points using $N_p = 2000$ particles (a) with and (b) without the energy spread, where the numerical errors are also indicated. As expected, the computation of W_y reaches the numerical convergence with much fewer particles than that of W_x. In addition, because of the extremely low emittance in the vertical direction, we find a characteristic "cross" (or "X") shape composed of a pair of ridges, each of which corresponds to the radiation from either of the two undulator segments. In contrast, we do not find a streak pattern as found in W_x, even if the energy spread is neglected, and the energy spread simply works to spoil the on-axis value, or the vertically projected brilliance, as shown in Fig. 4(b).

Now let us discuss the computation time needed for the above examples. Even with the state-of-the-art CPU (Intel Core i9-13900) and parallel computing using 12 MPI

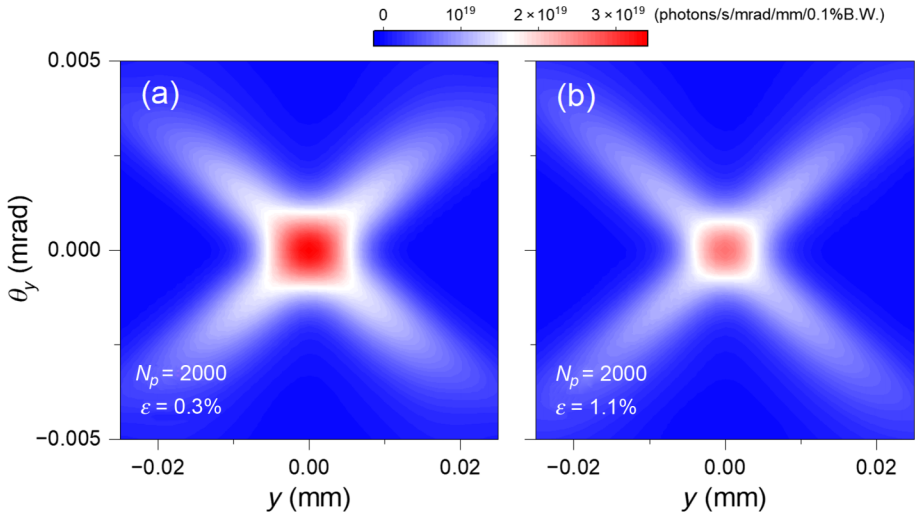


FIG. 4. Vertically projected Wigner functions evaluated by the Monte Carlo simulation with $N_p = 2000$. The energy spread is taken into account in (b) but not in (a).

(Message Passing Interface) processes, the Monte Carlo simulation to evaluate the 2D Wigner function shown in Figs. 3(f) and 4(b) takes more than $2 \times 10^4/500$ s. It is easy to imagine that we need a much longer time to evaluate the 4D Wigner function. For example, the Monte Carlo simulation with 2000 particles to evaluate the 4D Wigner function at 5^4 grid points (5 points for each axis of x, θ_x, y, and θ_y) requires more than 300 s; simply extrapolating the result to the grid points in the above example ($101 \times 81 \times 51^2$) and 64,000 particles, we find that more than a few months are needed to obtain a reliable result, which is obviously not feasible for practical applications.

It should be emphasized here that the computation in a normal (magnet-free) condition is much faster; for example, the computation of the Wigner function in the same condition as that discussed above, except that the two undulators are located in a magnet-free section and thus the beam waist is located solely at the origin, is completed within a second for the 2D function and 10 s even for the 4D one.

III. THEORETICAL APPROACH FOR FASTER COMPUTATION

In the preceding section, we have revealed the difficulty in computing the Wigner function in the MBW configurations; the straightforward Monte Carlo simulation requires an extremely long computation time. Let us now turn to the main subject of this paper and explore a theoretical approach to enable a faster computation.

A. Derivation of rigorous formulas

We first derive mathematical formulas to evaluate the Wigner function of UR emitted by an electron undergoing the betatron oscillation. Substituting Eqs. (4) and (9) into (10), the Wigner function can be decomposed as follows:

$$W = \sum_{i,j=1}^{N_u} w_{ij}, \tag{15}$$

with

$$w_{ij}(\boldsymbol{r},\boldsymbol{\theta}) = \frac{k^2}{4\pi^2}\int d\boldsymbol{\theta}' \mathrm{e}^{-ik\boldsymbol{\theta}'\cdot\boldsymbol{r}} \mathcal{E}_i^*\left(\boldsymbol{\theta}+\frac{\boldsymbol{\theta}'}{2}-\tilde{\boldsymbol{\beta}}_i\right)\mathcal{E}_j\left(\boldsymbol{\theta}-\frac{\boldsymbol{\theta}'}{2}-\boldsymbol{\beta}_j\right) \times \exp\left\{i(\phi_j-\phi_i)+ik\left[\tilde{\boldsymbol{r}}_i\cdot\left(\boldsymbol{\theta}+\frac{\boldsymbol{\theta}'}{2}\right)-\tilde{\boldsymbol{r}}_j\cdot\left(\boldsymbol{\theta}-\frac{\boldsymbol{\theta}'}{2}\right)\right]\right\}, \tag{16}$$

denoting the contribution from the ith and jth segments. It is easy to show $w_{ji} = w_{ij}^*$ and thus we have

$$W = \sum_{i=1}^{N_u} w_{ii} + 2\sum_{j>i}\mathrm{Re}(w_{ij}). \tag{17}$$

For convenience, w_{ii} is hereinafter referred to as the local Wigner function at the ith segment, while $w_{ij}(i \neq j)$ is referred to as the mutual Wigner function between the ith and jth segments.

To simplify the mathematical formulas in the following discussion, we focus on the variables in the horizontal phase space and omit those in the vertical one; extending the results to a more general case in the 4D phase space is straightforward.

Following the formulation presented in the former paper [7], we introduce normalized coordinate variables U and u defined as

$$U \equiv x/\chi, \qquad u \equiv \theta_x/\chi', \tag{18}$$

where χ and χ' are the positional and angular normalization factors satisfying the condition $\chi\chi' = \lambda/2\pi$. Note that each factor can be defined arbitrarily, as long as this condition is satisfied.

In a similar manner to U and u, we introduce normalized trajectory offsets at the ith undulator segment and lth subsection,

$$\tilde{U}_i \equiv \tilde{x}_i/\chi, \tilde{u}_i \equiv \tilde{\beta}_{xi}/\chi', \qquad U_l \equiv x_l/\chi, u_l \equiv \beta_{xl}/\chi'. \tag{19}$$

Note that U_0 and u_0 mean the normalized position and angle of the electron at the origin ($z = z_0 = 0$), and the trajectory offsets ($\tilde{U}_i$, $\tilde{u}_i$, U_l, and u_l) are given as a function of U_0 and u_0 through a transfer matrix representing the focusing magnet layout.

Using the normalized coordinate variables and trajectory offsets defined above, the local and mutual Wigner functions are given by

$$w_{ij}(U,u)=\frac{1}{2\pi}\int du' e^{-iUu'}\mathcal{E}_i^*\left(u+\frac{u'}{2}-\tilde{u}_i\right)\mathcal{E}_j\left(u-\frac{u'}{2}-\tilde{u}_j\right)\times\exp\left[i(\phi_j-\phi_i)+i\left(u+\frac{u'}{2}\right)\tilde{U}_i-i\left(u-\frac{u'}{2}\right)\tilde{U}_i\right],\tag{20}$$

where the phase terms ϕ_i and ϕ_j are also given as functions of U_0 and u_0, which is evident from their definitions in Eq. (8). Note that the coefficient $1/2\pi$ is introduced to satisfy the normalization as follows:

$$\int\int dUdu\, w_{ii}(U,u)=\int du|\mathcal{E}_i(u)|^2.\tag{21}$$

Introducing new variables defined as

$$\bar{U}=\frac{\tilde{U}_i+\tilde{U}_j}{2},\quad \bar{u}=\frac{\tilde{u}_i+\tilde{u}_j}{2},\quad \delta U=\tilde{U}_i-\tilde{U}_j,\quad \delta u=\tilde{u}_i-\tilde{u}_j.\tag{22}$$

Equation (20) reduces to

$$w_{ij}(U,u)=\frac{1}{2\pi}\int du'' e^{-iUu''}\Gamma_{ij}(u-\bar{u},u'')\exp(i\varphi),\tag{23}$$

with

$$\Gamma_{ij}(u,u'')=\mathcal{E}_i^*\left(u+\frac{u''}{2}\right)\mathcal{E}_j\left(u-\frac{u''}{2}\right),\tag{24}$$

and

$$\varphi=\phi_j-\phi_i+u\delta U+(\bar{U}-U)\delta u+u''\bar{U}.\tag{25}$$

Equation (23) defines the local and mutual Wigner functions formed by a single electron undergoing the betatron oscillation in the MBW configuration, whose coordinate variables at the origin are given by U_0 and u_0; we should pay attention to that $\bar{u}$ and φ in this equation are functions of U_0 and u_0, and Γ_{ij} depends on the electron energy.

For a realistic electron beam, we have to take into account the finite emittance and energy spread. Let us assume that the distribution function of the electron beam is defined as

$$P(U,u,\eta)=H(\eta)Q(U,u),\tag{26}$$

with

$$H(\eta)=\frac{1}{\sqrt{2\pi}\sigma_\eta}\exp\left(-\frac{\eta^2}{2\sigma_\eta^2}\right),\tag{27}$$

and

$$Q(U,u)=\frac{1}{2\pi\sigma_U\sigma_u}\exp\left[-\frac{(U+s_u u)^2}{2\sigma_U^2}-\frac{u^2}{2\sigma_u^2}\right],\tag{28}$$

where η is the energy deviation defined as $\eta=(\gamma-\gamma_0)/\gamma_0$ with γ_0 being the average energy, and σ_η is the energy spread. The parameters in $Q(U,u)$ specify the phase ellipse of the electron beam; if the dispersion function can be neglected, we have

$$\sigma_U=\frac{1}{\chi}\sqrt{\frac{\epsilon_x}{\gamma_x}},\quad \sigma_u=\frac{\sqrt{\epsilon_x\gamma_x}}{\chi'},\quad s_u=\frac{\alpha_x\chi'}{\gamma_x\chi},\tag{29}$$

where ϵ_x, α_x, and γ_x are the beam emittance and Twiss parameters in the horizontal direction. Then, the local and mutual Wigner functions for a realistic electron beam, W_{ij}, are given as

$$W_{ij}(U,u)=\int\int\int dU_0du_0d\eta\, P(U_0,u_0,\eta)w_{ij}(U,u),=\int\int dU_0du_0Q(U_0,u_0)\exp(i\varphi)\bar{w}(U,u-\bar{u}),\tag{30}$$

with

$$\bar{w}(U,u)=\frac{1}{2\pi}\int du'' e^{-iUu''}\bar{\Gamma}_{ij}(\sigma_\eta;u,u''),\tag{31}$$

$$\bar{\Gamma}_{ij}(\sigma_\eta;u,u'')=\frac{1}{\sqrt{2\pi}\sigma_\eta}\int d\eta\exp\left(-\frac{\eta^2}{2\sigma_\eta^2}\right)\Gamma_{ij}(u,u'').\tag{32}$$

Let us recall that $\bar{u}$ and φ in Eq. (30) are given as a function of U_0 and u_0, while Γ_{ij} in (32) depends on η. In other words, the effect of the finite emittance is described in Eq. (30), while that of the energy spread is in (32). Although Eq. (32) cannot be modified further and the computation should be done in this form, (30) can be reduced to a more convenient form for numerical operations. For this purpose, we change the integration variables from (U_0, u_0) to ($\bar{U}$, $\bar{u}$) using the relations

$$\begin{bmatrix}U_0\\u_0\end{bmatrix}=\bar{M}^{-1}\begin{bmatrix}\bar{U}\\\bar{u}\end{bmatrix}\equiv\begin{bmatrix}\nu_0&\nu_1\\\nu_2&\nu_3\end{bmatrix}\begin{bmatrix}\bar{U}\\\bar{u}\end{bmatrix},\tag{33}$$

and

$$\begin{bmatrix} \delta U \\ \delta u \end{bmatrix} = \delta M \bar{M}^{-1} \begin{bmatrix} \bar{U} \\ \bar{u} \end{bmatrix} \equiv \begin{bmatrix} \mu_0 & \mu_1 \\ \mu_2 & \mu_3 \end{bmatrix} \begin{bmatrix} \bar{U} \\ \bar{u} \end{bmatrix}, \tag{34}$$

where $\bar{M}$ and δM are the transfer matrices derived in Appendix A, and we have introduced ν and μ to represent their elements.

Substituting Eqs. (33) and (34) into (30), we have

$$W_{ij}(U,u) = W_0 \int\int d\bar{U} d\bar{u}\, \bar{w}(U-\bar{U}, u-\bar{u}) \exp[\Theta(\bar{U},\bar{u},U,u)], \tag{35}$$

with

$$\begin{aligned} W_0 &= \frac{|\bar{M}^{-1}|}{2\pi\sigma_U\sigma_u}, \\ \Theta(\bar{U},\bar{u},U,u) &= -G(\bar{U},\bar{u}) + ig(\bar{U},\bar{u}) + if(\bar{U},\bar{u},U,u) \\ G(\bar{U},\bar{u}) &= \frac{[(\nu_0+s_u\nu_2)\bar{U} + (\nu_1\bar{u}+s_u\nu_3)\bar{u}]^2}{2\sigma_U^2} + \frac{(\nu_2\bar{U}+\nu_3\bar{u})^2}{2\sigma_u^2}, \\ g(\bar{U},\bar{u}) &= \phi_j(\bar{U},\bar{u}) - \phi_i(\bar{U},\bar{u}) + \mu_2\bar{U}^2 + \mu_3\bar{u}\,\bar{U}, \\ f(\bar{U},\bar{u},U,u) &= -(\mu_3\bar{u}+\mu_2\bar{U})U + (\mu_1\bar{u}+\mu_0\bar{U})u, \end{aligned} \tag{36}$$

where the phase terms ϕ_i and ϕ_j are determined by Eq. (8) as a summation of the square of the angular offset at relevant subsections; because all of them are given as a linear combination of x_0 and β_{x0}, ϕ_i and ϕ_j are defined by a quadratic form of $\bar{U}$ and $\bar{u}$ as well as other terms in $G(\bar{U},\bar{u})$ and $g(\bar{U},\bar{u})$.

Equation (35) raises a critical problem in computing the distribution of W_{ij} on the phase space (U,u). Namely, we cannot apply the convolution method, because the function Θ, or more specifically f, depends not only on $\bar{U}$ and $\bar{u}$ but also on U and u; this means that the computation of W_{ij} should be repeated for each coordinate grid point (U,u), which can potentially require a long computation time. In this regard, it should be emphasized that g and f vanish if $i=j$, and Eq. (35) reduces to a simple convolution integral. In other words, the distribution of the local $(i=j)$ Wigner function can be computed much faster than that of the mutual $(i\neq j)$ one. Thus, we should explore a theoretical approach to compute the distribution of the mutual Wigner function in a more efficient manner to aim at a faster computation.

B. Semianalytical solution for a Gaussian beam

As a first step toward the more efficient computation of the mutual Wigner function, we consider a Gaussian beam; in this case, the integration in Eq. (35) can be done in a semianalytical manner as follows:

Let us assume that the complex amplitude of radiation emitted at each undulator is identically given by a Gaussian function defined as

$$\mathcal{E}_0(u) = \frac{1}{\sqrt[4]{2\pi}\sqrt{\Sigma_u}} \exp\left(-\frac{u^2}{4\Sigma_u^2}\right), \tag{37}$$

with

$$\Sigma_u = \frac{1}{\chi'}\sqrt{\frac{\lambda}{2L_u}}, \tag{38}$$

denoting the normalized angular divergence of radiation, which is derived from the well-known formula for the angular divergence of UR with the undulator length L_u. Note that $\mathcal{E}_0$ is normalized as

$$\int du |\mathcal{E}_0(u)|^2 = 1. \tag{39}$$

For later discussions, we define the normalized source size of radiation Σ_U. Recalling the relation $\chi\chi' = \lambda/2\pi$ and the diffraction-limited emittance of $\lambda/4\pi$, we have $\Sigma_U\Sigma_u = 1/2$.

It should be emphasized that $\mathcal{E}_0$ denotes the complex amplitude at the center of each undulator (i.e., $z = Z_i \equiv \frac{Z_{u,i}+Z_{d,i}}{2}$), but not at the origin ($z=0$). To transfer

from $z = Z_i$ to $z = 0$, we have to multiply a phase factor $\exp(ikZ_i\boldsymbol{\theta}^2/2)$ to describe the diffraction effect, which yields

$$\mathcal{E}_i(u) = \frac{1}{\sqrt[4]{2\pi}\sqrt{\Sigma_u}}\exp\left(-\frac{u^2}{4\Sigma_u^2}\right)\exp\left(\frac{ikZ_i\chi'^2u^2}{2}\right). \quad (40)$$

Substituting into Eq. (31) and neglecting the energy spread, $\bar{w}$ reduces to

$$\bar{w}(U,u) = \bar{w}_G(U,u) \equiv \frac{\psi}{2\pi\Sigma_U\Sigma_u}\exp\left[-\frac{\psi^2(U+\hat{Z}u)^2}{2\Sigma_U^2} - \frac{u^2}{2\psi^2\Sigma_u^2}\right], \quad (41)$$

with

$$\hat{Z} = k\frac{Z_i + Z_j}{2}\chi'^2, \quad (42)$$

$$\psi^2 = \frac{1}{1 + ik(Z_i - Z_j)\chi'^2\Sigma_u^2}, \quad (43)$$

where $\hat{Z}$ denotes the normalized midpoint between the ith and jth undulator segments. Note that $\bar{w}_G$ represents the mutual Wigner function formed by two Gaussian beams whose source points are located at $z = Z_i$ and $z = Z_j$. It should also be emphasized that the integral of $\bar{w}_G$ over the whole phase space reduces to ψ, namely

$$\psi = \int\int dU du\, \bar{w}_G(U,u). \quad (44)$$

Substituting Eq. (41) into (35), we have

$$W_{ij}(U,u) = W_0\frac{\psi}{\pi}\int\int d\bar{U}d\bar{u}\exp[\Phi(\bar{U},\bar{u},U,u)], \quad (45)$$

with

$$\Phi(\bar{U},\bar{u},U,u) = -\frac{\psi^2[U-\bar{U}+\hat{Z}(u-\bar{u})]^2}{2\Sigma_U^2} - \frac{(u-\bar{u})^2}{2\psi^2\Sigma_u^2} - G(\bar{U},\bar{u}) + ig(\bar{U},\bar{u}) + if(\bar{U},\bar{u},U,u). \quad (46)$$

The integration in Eq. (45) can be done semianalytically as discussed in Appendix B, and we have

$$W_{ij}(U,u) = W_0\frac{2\psi}{\sqrt{4AB-C^2}}\exp\left(-\frac{BD^2 - CDE + AE^2}{4AB-C^2} + F\right), \quad (47)$$

with the parameters $A-F$ being derived in Appendix B.

Having derived the analytical formula of W_{ij} for a Gaussian beam, let us discuss the impact of the finite emittance on the mutual Wigner function. As an example, we assume the configurations and parameters in the former example, and two undulator segments are considered again. This means that we have just one combination $(i,j) = (1,2)$ to form the mutual Wigner function. Figure 5(a) shows $\bar{w}$, or the mutual Wigner function without the effect of the finite emittance, computed with Eq. (41) and plotted on the 2D phase space. Note that U and u are normalized by the source size Σ_U and angular spread Σ_u of the Gaussian beam, while $\bar{w}$ is normalized by its maximum value. Figure 5(a′) is the same as Fig. 5(a), but both scales are expanded to facilitate visualization near the axis. The characteristic pattern is attributable to the phase factor $\exp(ikZ_i\boldsymbol{\theta}^2/2)$ describing the diffraction effect.

Now, let us turn to the effect of the finite emittance. For reference, the phase ellipses of the electron beam defined by the distribution function $Q(U,u)$ in the horizontal and vertical directions are indicated by the solid lines (as 1σ) in Figs. 5(a) and 5(a′), respectively. Figures 5(b) and 5(c) show W_{ij} computed with Eq. (47), assuming the emittance and betatron function in the horizontal and vertical directions, as used in the computations shown in Figs. 3 and 4, respectively. Again, W_{ij} is normalized by the maximum value of $\bar{w}$ in both figures.

Because of the large emittance, the horizontal phase ellipse shown in Fig. 5(a) is much larger than the area occupied by $\bar{w}$. If W_{ij} is simply given by the convolution of $\bar{w}$ and Q, it will reduce to a 2D Gaussian function whose widths are similar to those of Q. In practice, however, this is not correct as found in Fig. 5(b); the overall profile of W_{ij} is completely different from Q, and significantly shrinks along the U axis. This means that most of the electrons injected with finite positional offsets do not contribute to the formation of the mutual Wigner function.

In contrast to the horizontal direction discussed above, the vertical phase ellipse of the electron beam is rather smaller than the area occupied by $\bar{w}$ as shown in Fig. 5(a′). As a result, the characteristic pattern found in Fig. 5(a′) remains well even with the effect of the finite emittance as found in Fig. 5(c).

C. Quasiconvolution

In the preceding section, we have examined the impact of the finite emittance on the mutual Wigner function

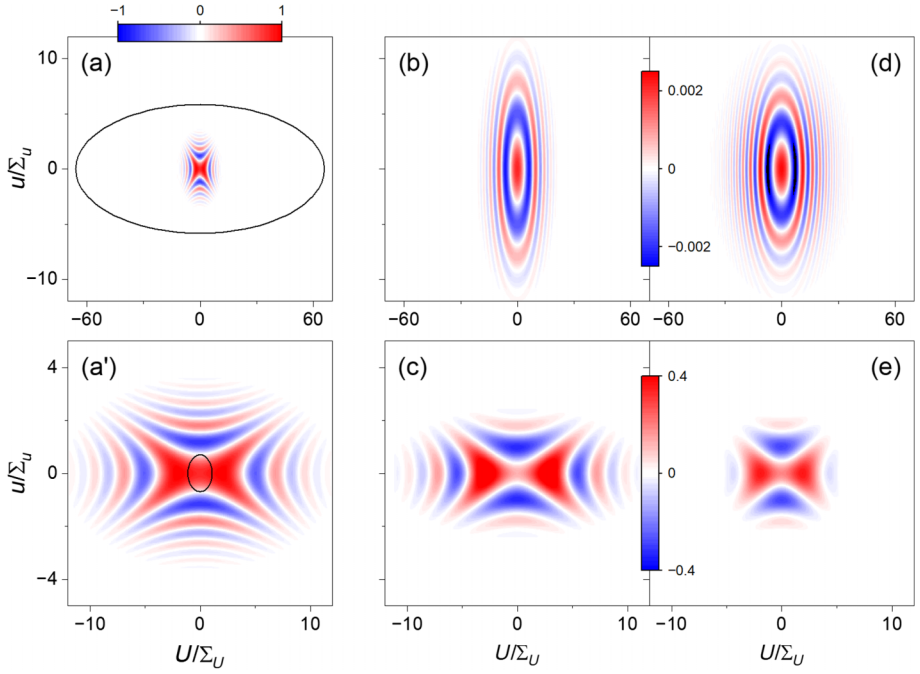


FIG. 5. Mutual Wigner functions computed with different electron beam parameters and numerical methods: (a), (a′) $\bar{w}$ with Eq. (41), (b), (c) W_{ij} with Eq. (47), and (d), (e) $\tilde{W}_{ij}$ with Eq. (48). Electron beam parameters used in the computation of W_x (Fig. 3) and W_y (Fig. 4) are assumed in (b), (d) and (c), (e), respectively. The solid lines in (a) and (a′) indicate the phase ellipses of the electron beam in the horizontal and vertical directions.

under the assumption that UR is a Gaussian beam. We now explore a numerical method to accelerate the computation of the distribution of W_{ij}. To be more specific, we look for an alternative (or approximate) mathematical form of Eq. (35); obviously, it should reproduce the results by the rigorous numerical methods as much as possible.

Putting aside the reason for now, let us introduce a function $\tilde{W}_{ij}$ as an approximate form of W_{ij}, which is defined as

$$\tilde{W}_{ij}(U,u) \equiv W_0 \int\int d\bar{U}d\bar{u}\,\bar{w}(U-\bar{U},u-\bar{u})\exp[\tilde{\Theta}(p,q;\bar{U},\bar{u})], \tag{48}$$

with

$$\begin{aligned}\tilde{\Theta}(p,q;\bar{U},\bar{u}) &= \Theta(\bar{U},\bar{u},\bar{U},\bar{u}) \\ &\quad -\frac{p^2}{2}(\mu_3\bar{u}+\mu_2\bar{U})^2 - \frac{q^2}{2}[(\mu_1+\mu_3\hat{Z})\bar{u}+(\mu_0+\mu_2\hat{Z})\bar{U}].\end{aligned} \tag{49}$$

The difference between W_{ij} in Eq. (35) and $\tilde{W}_{ij}$ in (48) is that the coordinate variables U and u are not contained in the exponent of the integrand in the latter; in other words, it takes the form of a convolution integral and thus the computation of the distribution of $\tilde{W}_{ij}$ can be orders of magnitude faster than that of W_{ij}, depending on the number of the grid points in (U,u). In this approximation, we have two issues to be addressed: how well $\tilde{W}_{ij}$ reproduces W_{ij}, and how to optimize the parameters p and q.

To discuss the above issues, let us first consider the integral of $\tilde{W}_{ij}$ and W_{ij} over the whole phase space, which is hereinafter referred to as the mutual photon flux. It is easy to show

$$\begin{aligned}\tilde{\Psi}_{ij} &\equiv \int\int dUdu\,\tilde{W}_{ij}(U,u) \\ &= W_0 \int\int d\bar{U}d\bar{u}\exp[\tilde{\Theta}(p,q;\bar{U},\bar{u})]\int\int dUdu\,\bar{w}(U,u),\end{aligned} \tag{50}$$

and

$$\Psi_{ij} \equiv \int\int dUdu\, W_{ij}(U,u) = W_0 \int\int d\bar{U}d\bar{u} \exp\left[\Theta(\bar{U},\bar{u},\bar{U},\bar{u})\right] \int\int dUdu\, \bar{w}(U,u) \exp\left[if(\bar{U},\bar{u},U,u)\right]. \tag{51}$$

In the case of a Gaussian beam discussed in the preceding section, the integration over (U,u) in Eq. (51) can be analytically done to yield

$$\int\int dUdu\bar{w}_G(U,u)\exp\left[if(\bar{U},\bar{u},U,u)\right] = \psi \exp\left\{-\frac{\Sigma_U^2}{2\psi^2}(\mu_3\bar{u}+\mu_2\bar{U})^2 - \frac{\psi^2\Sigma_u^2}{2}\left[(\mu_1+\mu_3\hat{Z})\bar{u}+(\mu_0+\mu_2\hat{Z})\bar{U}\right]\right\}. \tag{52}$$

Then we have

$$\Psi_{ij} = W_0\psi \int\int d\bar{U}d\bar{u} \exp\left[\tilde{\Theta}\left(\frac{\Sigma_U}{\psi}, \psi\Sigma_u; \bar{U},\bar{u}\right)\right] = W_0 \int\int dUdu\, \bar{w}_G(U,u) \int\int d\bar{U}d\bar{u} \exp\left[\tilde{\Theta}\left(\frac{\Sigma_U}{\psi}, \psi\Sigma_u; \bar{U},\bar{u}\right)\right], \tag{53}$$

where Eq. (44) has been used to derive the last equation. Comparing Eqs. (50) and (53), it is obvious that $\tilde{\Psi}_{ij}$ reduces to Ψ_{ij} for a Gaussian beam, when p and q satisfy the conditions

$$p = \frac{\Sigma_U}{\psi}, \qquad q = \psi\Sigma_u. \tag{54}$$

The above discussion for a Gaussian beam ($\bar{w} \to \bar{w}_G$) suggests that $\tilde{W}_{ij}$ can be a good alternative to W_{ij}, if the parameters p and q are optimized as in Eq. (54).

To further examine the above result, let us consider an extreme case when Σ_U and Σ_u approach 0 at the same time. Although this condition cannot be satisfied in reality because of the relation $\Sigma_U\Sigma_u = 1/2$ describing the diffraction of radiation, we proceed anyway to investigate how $\tilde{W}_{ij}$ and W_{ij} behave in this extreme condition in a mathematical sense. Then $\bar{w}(U,u)$ reduces to a 2D delta function, namely $\bar{w}(U,u) \to \delta(U,u)$, and we have

$$\begin{aligned} W_{ij}(U,u) &\to W_0 \exp[\Theta(U,u,U,u)] \equiv G_{ij}(U,u), \\ \tilde{W}_{ij}(U,u) &\to W_0 \exp[\tilde{\Theta}(0,0;U,u)] \equiv \tilde{G}_{ij}(U,u). \end{aligned} \tag{55}$$

Recalling the condition supposed in deriving the above formulas, we may call G_{ij} and $\tilde{G}_{ij}$ Green's functions or point spread functions in the phase space (U,u). Because of a relation $\Theta(U,u,U,u) = \tilde{\Theta}(0,0;U,u)$, G_{ij} and $\tilde{G}_{ij}$ are identical in practice, and thus $\tilde{W}_{ij}$ reduces to W_{ij} in this extreme condition $\Sigma_U \to 0$ and $\Sigma_u \to 0$.

Although the above mathematical operations suggest the validity of $\tilde{W}_{ij}$ as an approximate form of W_{ij} in terms of the mutual photon flux and Green's function, we have another point to be addressed, namely, the mutual brilliance, or the on-axis value of the mutual Wigner function $W_{ij}(0,0)$. Although the condition (54) guarantees the consistency in the mutual photon flux Ψ_{ij}, it does not necessarily mean the consistency in the mutual brilliance $W_{ij}(0,0)$. To tackle this issue, we consider an alternative condition

$$p = \hat{p}\frac{\Sigma_U}{\psi}, \qquad q = \hat{q}\psi\Sigma_u, \tag{56}$$

and optimize $\hat{p}$ and $\hat{q}$ to improve the consistency both in the mutual photon flux and brilliance. For this purpose, we have to define an objective function $\mathcal{O}(\hat{p},\hat{q})$ to evaluate the consistency between Ψ_{ij} and $\tilde{\Psi}_{ij}$ as well as $W_{ij}(0,0)$ and $\tilde{W}_{ij}(0,0)$, and optimize $\hat{p}$ and $\hat{q}$ to maximize $\mathcal{O}$. Among a number of possible options, we propose an objective function defined as

$$\mathcal{O}(\hat{p},\hat{q}) = \left[\left|\frac{\Psi_{ij}-\tilde{\Psi}_{ij}}{\psi W_0}\right|^2 + \left|\frac{W_{ij}(0,0)-\tilde{W}_{ij}(0,0)}{W_{ij}(0,0)}\right|^2\right]^{-1}, \tag{57}$$

where the first and second terms denote the consistencies in the mutual photon flux and brilliance, respectively. Using the objective function defined above, the parameters $\hat{p}$ and $\hat{q}$ can be easily determined by means of a general method for numerical optimization. Note that the objective function $\mathcal{O}$ for a given set of $(\hat{p},\hat{q})$ can be easily and quickly evaluated by computing the respective terms (Ψ_{ij}, $\tilde{\Psi}_{ij}$, W_{ij}, and $\tilde{W}_{ij}$) for a Gaussian beam, using the semi-analytical method presented in Sec. III B.

Now let us show the consistency between the rigorous expression W_{ij} and approximate form $\tilde{W}_{ij}$. As an example, we computed $\tilde{W}_{ij}$ in the two conditions assumed in the computation of W_{ij} shown in Figs. 5(b) and 5(c); the

results are shown in Figs. 5(d) and 5(e), where the parameters $\hat{p}$ and $\hat{q}$ are optimized by the procedure explained above as follows: $(\hat{p},\hat{q}) = (1.01, 1.00)$ in (d) and $(1.00, 2.82)$ in (e). We find a good agreement between W_{ij} (b) and (c) and $\tilde{W}_{ij}$ (d) and (e), particularly near the axis $(U,u) = (0,0)$.

The above examples definitely validate the numerical method introduced in this section, which is referred to as a "quasiconvolution" method. The advantage is that, as already mentioned, Eq. (48) has the form of a convolution integral, and thus computing its distribution in the (U,u) phase space can be much faster than that with the rigorous method using Eq. (35).

D. Decay factor of the mutual Wigner function

In the former sections, we have discussed the numerical method to compute the mutual Wigner functions, which usually takes a much longer time than computing the local ones. To overcome this issue, the quasiconvolution method has been introduced. In this section, we discuss another issue which may further reduce the numerical cost; recalling that the Wigner function is given as a sum of all the local and mutual Wigner functions, we can skip the computation of the mutual Wigner functions, if their contributions are much lower than those from the local ones. In practice, the finite emittance and energy spread have a larger impact on the mutual Wigner function than on the local one, and thus the contribution from the former decays more rapidly. In this regard, it is reasonable to introduce a "decay factor," which is defined by the contribution from a specific mutual Wigner function relative to that from the local one.

Strictly speaking, we have to compute both the (mutual and local) Wigner functions to examine their exact contributions and evaluate the decay factor, which does not make sense to reduce the numerical cost. It is worth noting, however, that roughly estimating the ratio of the mutual and local Wigner functions can be done easily, once relevant conditions are given, such as the emittance and energy spread of the electron beam. In what follows, we present a simple method to evaluate the decay factor to judge whether the computation of a specific mutual Wigner function can be skipped.

Let us first discuss the effect of the finite emittance; for this purpose, we have to extend the 2D formula for the mutual Wigner function to a more general 4D one. The 2D function $\bar{w}(U,u)$ in Eq. (48) should be replaced by a 4D function $\bar{w}(U,u,V,v)$, where V and v are the normalized coordinates in the vertical direction defined in the same manner as U and u. In addition, another exponential factor describing the vertical emittance effect should be multiplied. Following the semianalytical treatment in Sec. III B, it is reasonable to consider a Gaussian beam, because our current goal is to roughly evaluate the decay factor. Then, we have

$$\bar{w}(U,u,V,v) = \bar{w}_G(U,u)\bar{w}_G(V,v), \tag{58}$$

which yields

$$W_{ij}(U,u,V,v) = W_{Uij}(U,u)W_{Vij}(V,v), \tag{59}$$

where W_{Uij} is the 2D mutual Wigner function in the (U,u) phase space defined in (35), while W_{Vij} is the same as W_{Uij} but defined in the (V,v) phase space. Substituting into Eq. (12), the 2D projected mutual Wigner functions $\mathcal{W}_{Uij}$ and $\mathcal{W}_{Vij}$ are given as

$$\begin{aligned}\mathcal{W}_{Uij}(U,u) &\equiv \int\int \tilde{W}_{ij}(U,u,V,v)dVdv = \Psi_{Vij}W_{Uij}(U,u),\\ \mathcal{W}_{Vij}(V,v) &\equiv \int\int \tilde{W}_{ij}(U,u,V,v)dUdu = \Psi_{Uij}W_{Vij}(V,v).\end{aligned} \tag{60}$$

In the above formulas, it should be emphasized that the 2D mutual Wigner function (W_{Uij}, W_{Vij}) and mutual photon flux (Ψ_{Uij}, Ψ_{Vij}) can be easily evaluated by the semianalytical method as presented in Sec. III B.

To evaluate the contributions from the mutual and local Wigner functions, it is reasonable to pick up their maximum values; namely, the decay factor is defined as the ratio of the on-axis value of the mutual Wigner function to that of the local one. For example, it is given as

$$\rho = \frac{W_{ij}(0,0,0,0)}{W_{ii}(0,0,0,0)}, \tag{61}$$

for the computation of the 4D Wigner function, and

$$\rho_U = \frac{\mathcal{W}_{Uij}(0,0)}{\mathcal{W}_{Uii}(0,0)}, \qquad \rho_V = \frac{\mathcal{W}_{Vij}(0,0)}{\mathcal{W}_{Vii}(0,0)}, \tag{62}$$

for that of the 2D projected Wigner functions. Assuming the parameters in Table I, we find $\rho = 0.11$, $\rho_U = 0.059$, and $\rho_V = 8.8 \times 10^{-3}$; these values suggest that the mutual Wigner function has a negligible contribution in the vertically projected Wigner function (W_y), but has some impacts on the computation of horizontally projected (W_x) and 4D (W) Wigner functions. This is actually verified in

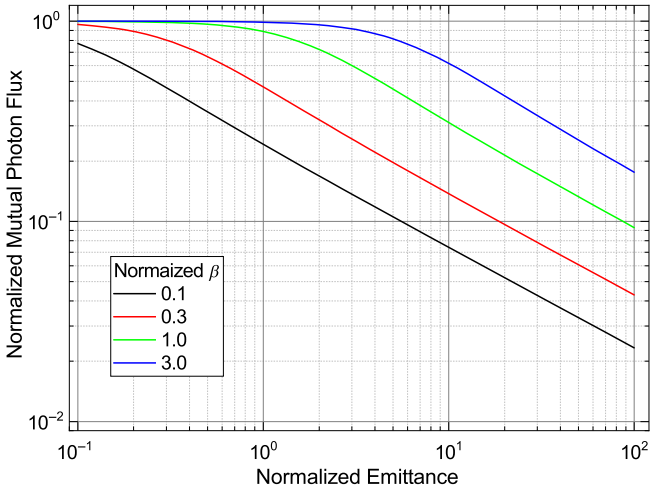


FIG. 6. Mutual Wigner function plotted as a function of the normalized emittance.

the result by the Monte Carlo simulation shown in Fig. 3(e), where the central fringe pattern definitely shows the contribution from the mutual Wigner function.

To examine how the emittance and betatron function contribute to the decay factor, we computed the mutual photon flux for the two-segment condition and plotted in Fig. 6; note that the mutual flux is normalized by that without the emittance, the emittance is normalized by that of diffraction-limited light ($\lambda/4\pi$), and the betatron function is normalized by the length of the undulator segment (L_u). The mutual photon flux decays more rapidly for larger emittances and smaller betatron functions (stronger focusing) as expected.

Next, the effect of the energy spread is discussed; for this purpose, we have to rewrite Eq. (24) to include explicitly the energy deviation η. Let us consider an electron without positional and angular offsets, but with an energy $\gamma = \gamma_0(1+\eta)$ different from that of the reference electron (γ_0). Assuming that this electron passes through the origin ($z = 0$) at the same time as the reference electron, the difference in time for the two electrons to arrive at the center of the ith undulator segment is given as

$$\Delta t_i(\eta) = \left(\frac{1}{2\gamma^2 c} - \frac{1}{2\gamma_0^2 c}\right)\int_0^{z_i}[1+\gamma_0^2\langle\boldsymbol{\beta}\rangle^2(z)]dz, \quad (63)$$

which results in a phase shift $ck\Delta t_i$ in the complex amplitude $\mathcal{E}_i$, with c being the speed of light. Then, we have

$$\Gamma_{ij}(u,u'') = \mathcal{E}_i^*\left(u+\frac{u''}{2}\right)\mathcal{E}_j\left(u-\frac{u''}{2}\right)\exp(-2ik\eta\Lambda_{ij}), \quad (64)$$

with

$$\Lambda_{ij} = \frac{1}{2\gamma_0^2}\int_{z_i}^{z_j}[1+\gamma_0^2\langle\boldsymbol{\beta}\rangle^2(z)]dz, \quad (65)$$

being known as the slippage length. Substituting Eqs. (64), (32) reduces to

$$\bar{\Gamma}_{ij}(\sigma_\eta;u,u'') = \frac{1}{\sqrt{2\pi}\sigma_\eta}\int d\eta\exp\left(-\frac{\eta^2}{2\sigma_\eta^2} - 2ik\eta\Lambda_{ij}\right)\mathcal{E}_i^*\left(u+\frac{u''}{2}\right)\mathcal{E}_j\left(u-\frac{u''}{2}\right). \quad (66)$$

In general, the integration in the above equation cannot be done analytically, because the complex amplitude $\mathcal{E}_i$ depends on η as well as the exponential factor. Nevertheless, we can roughly evaluate the effect of the energy spread by factoring out $\mathcal{E}_i^*\mathcal{E}_j$ from the integral, which yields

$$\bar{\Gamma}_{ij}(\sigma_\eta;u,u'') \sim \mathcal{E}_i^*\left(u+\frac{u''}{2}\right)\mathcal{E}_j\left(u-\frac{u''}{2}\right)\rho_\eta, \quad (67)$$

with

$$\rho_\eta = \exp(-2\sigma_\eta^2 k^2\Lambda_{ij}^2) \quad (68)$$

denoting the effect of the energy spread, meaning that the mutual Wigner function decays exponentially as the growth of Λ_{ij} and σ_η. Note that the above formula can be modified to a convenient form

$$\rho_\eta = \exp(-2\hat{\sigma}_\eta^2), \quad (69)$$

with

$$\hat{\sigma}_\eta = 2\pi n_h(j-i)(N_u+N_d)\sigma_\eta \quad (70)$$

denoting the normalized energy spread, where N_u denotes the number of undulator periods, $n_h = \lambda_1/\lambda$ is the harmonic number with λ_1 being the fundamental wavelength of UR, and N_d denotes the number of slippage in the drift section defined as

$$N_d = \frac{L-L_u}{2\gamma_0^2\lambda_1}. \quad (71)$$

The above formula indicates that, because of the finite energy spread of the electron beam, the mutual Wigner function decays more rapidly for higher harmonics (n_h),

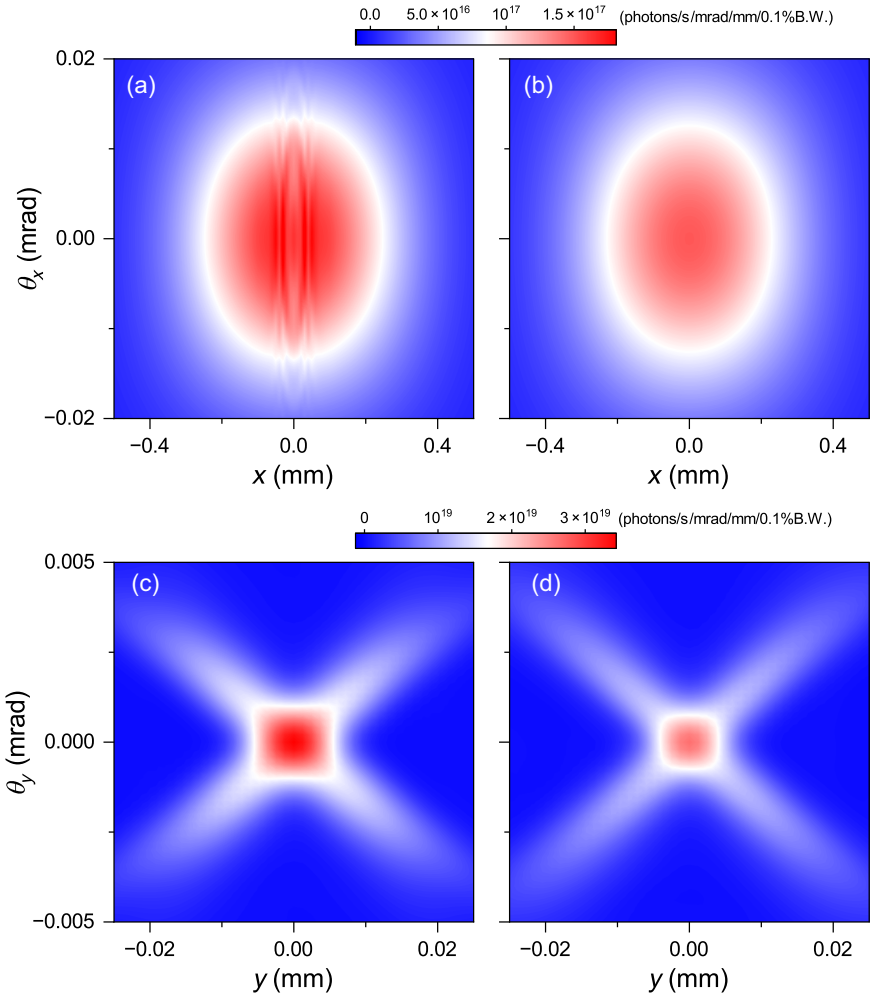


FIG. 7. Wigner functions projected on the horizontal (a), (b) and vertical (c), (d) phase spaces, computed by the FC method with the parameters used in Figs. 3 and 4. The energy spread is taken into account in (b), (d) but not in (a), (c).

more undulator periods (N_u), and longer interval between segments (longer L and larger $|j-i|$).

Assuming the parameters in Table I, we find $\rho_\eta = 9.1 \times 10^{-8}$; thus, we can skip the computation of the mutual Wigner function unless we neglect the effect of the energy spread. Note that this is consistent with the results by the Monte Carlo simulation shown in Figs. 3(e) and 3(f), where the characteristic fringe pattern disappears when the energy spread is taken into account.

Needless to say, we have to multiply the decay factors denoting the finite emittance (ρ etc.) and energy spread (ρ_η), and set up a threshold below which the computation of the mutual Wigner function can be skipped. It is worth noting that if the decay factors are extremely low as in the above example, all the undulators can be regarded as completely independent light sources.

IV. COMPARISON WITH THE MONTE CARLO SIMULATION

In the former sections, we presented the quasiconvolution method and introduced the decay factors to reduce the numerical cost in computing the Wigner function in the MBW configuration. The computation of Wigner functions based on the two methods can be potentially much faster than the Monte Carlo simulation, which is thus hereinafter referred to as a "fast computation" (FC) method. To examine its validity, we computed the projected Wigner functions by the FC method with the parameters used in Figs. 3 and 4. As an example, the threshold decay factor has been set to 10^{-3}. The results are shown in Figs. 7(a)–7(d), where (a) and (b) show the horizontally projected Wigner function W_x, while (c) and (d) show the vertical one W_y. Note that the energy spread is taken into account in (b) and (d), but not in (a) and (c).

TABLE II. Comparison between the Monte Carlo (MC) simulation and FC method. Note that the projected brilliance ($\mathcal{B}_{x,y}$) is given in the unit of photons/s/mm/mrad/0.1%B.W.

Method	MC	FC	MC	FC
Energy spread	Without		With	
$\mathcal{B}_x$	1.61×10^{17}	1.57×10^{17}	1.47×10^{17}	1.45×10^{17}
ζ_x	3.02×10^{-3}	3.05×10^{-3}	2.83×10^{-3}	2.87×10^{-3}
τ_x (s)	11,000	13	24,000	2.5
$\mathcal{B}_y$	3.38×10^{19}	3.37×10^{19}	2.64×10^{19}	2.72×10^{19}
ζ_y	0.367	0.377	0.320	0.332
τ_y (s)	310	3.7	510	4.1

Thus, W_x shown in Figs. 7(a) and 7(b) is to be compared with Figs. 3(e) and 3(f), while W_y in Figs. 7(c) and 7(d) is with Figs. 4(a) and 4(b). All of the computation results by the FC method well reproduce those by the Monte Carlo simulation; for example, the characteristic fringe pattern in the center is found in Fig. 7(a) and disappears in Fig. 7(b).

To compare the two methods in a more quantitative manner, Table II summarizes the brilliance $\mathcal{B}_{x,y} = W_{x,y}(0,0)$ and overall degree of coherence $\zeta_{x,y}$ defined as [10]

$$\zeta_x = \lambda \frac{\int\int dx d\theta_x W_x^2(x,\theta_x)}{[\int\int dx d\theta_x W_x(x,\theta_x)]^2}, \tag{72}$$

and a similar expression for ζ_y. Note that "MC" and "FC" stand for the Monte Carlo simulation and FC method, respectively. The results by the two different methods agree well in each item, both in the large-emittance (W_x) and low-emittance (W_y) conditions, supporting the validity of the FC method presented in this paper.

Finally, let us compare the computation time as summarized in Table II as well, where $\tau_{x,y}$ denotes the time needed for the computation of $W_{x,y}$ under the computing environment mentioned in Sec. II C; we find that the FC method is 2–4 orders of magnitude faster than that of the conventional Monte Carlo simulation to evaluate the projected Wigner functions. It is obvious that this kind of significant reduction in the computation time is also expected in the 4D Wigner function, which is not realistic by the Monte Carlo simulation as mentioned in Sec. II C. For example, computing the 4D Wigner function by means of the FC method with the same parameters and conditions (grid points and computing environment) as those used so far is completed within a minute, which is short enough for practical applications.

It is worth noting that the comparison between the MC simulation and FC method has been made in Appendix C using other parameters, where the validity and capability of the FC method are verified again.

V. SUMMARY

We presented a numerical method to compute the Wigner function of UR when the magnet-free assumption is violated and the conventional convolution method is not applicable. The examples presented in the preceding section have revealed that the proposed method significantly reduces the numerical cost in computing the Wigner functions in the MBW configuration, without sacrificing the reliability and accuracy of computation. Note that the numerical method has been implemented in the SR calculation code *SPECTRA* [11], which is freely available online.

Before closing, let us discuss the limitations of the method; the only assumption is that the whole section can be divided into a number of subsections within which the magnet-free assumption is valid and the electron travels along a straight line besides the sinusoidal motion. A typical example to violate this assumption is the undulator natural focusing, in which an electron beam is focused while it travels along the undulator; as a result, electrons with positional/angular offsets are gradually deflected and thus their trajectories become parabolic or sinusoidal according to the conditions such as the electron energy and the magnetic field of the undulator. It is obvious that the numerical method presented in this paper cannot be applied in such a case. One solution is to divide the undulator into many subsections so that the betatron phase advance within a single subsection is small enough; then, the parabolic and/or sinusoidal trajectory of each electron can be well approximated by a polygon and the magnet-free assumption is valid within respective sides of the polygon.

DATA AVAILABILITY

There are no publicly available research data or software supporting this manuscript. Requests for further information or data should be sent to the authors.

APPENDIX A: TRANSFER MATRIX FOR THE NORMALIZED COORDINATE

It is well known that the motion of an electron undergoing betatron oscillation, apart from the sinusoidal motion in the undulator, is simply given by a transfer matrix

$$\begin{bmatrix} x(z) \\ \beta_x(z) \end{bmatrix} = \begin{bmatrix} C(z) & S(z) \\ C'(z) & S'(z) \end{bmatrix} \begin{bmatrix} x(0) \\ \beta_x(0) \end{bmatrix}, \tag{A1}$$

where the elements of the matrix are determined by the focusing magnet layout. At the entrance of the ith undulator $z = Z_{u,i}$, we have

$$\begin{bmatrix} x(Z_{u,i}) \\ \beta_x(Z_{u,i}) \end{bmatrix} = \begin{bmatrix} \tilde{x}_i + \tilde{\beta}_{xi} Z_{u,i} \\ \tilde{\beta}_{xi} \end{bmatrix} = \begin{bmatrix} C_i & S_i \\ C_i' & S_i' \end{bmatrix} \begin{bmatrix} x_0 \\ \beta_{x0} \end{bmatrix}, \quad \text{(A2)}$$

where $C_i = C(Z_{u,i})$ and so on. It is easy to show

$$\begin{bmatrix} \tilde{x}_i \\ \tilde{\beta}_{xi} \end{bmatrix} = \begin{bmatrix} C_i - C_i' Z_{u,i} & S_i - S_i' Z_{u,i} \\ C_i' & S_i' \end{bmatrix} \begin{bmatrix} x_0 \\ \beta_{x0} \end{bmatrix}, \quad \text{(A3)}$$

which reduces to the transfer matrix in the normalized coordinate,

$$\begin{bmatrix} U_i \\ u_i \end{bmatrix} = \begin{bmatrix} C_i - C_i' Z_{u,i} & (S_i - S_i' Z_{u,i})\chi'/\chi \\ C_i' \chi/\chi' & S_i' \end{bmatrix} \begin{bmatrix} U_0 \\ u_0 \end{bmatrix} = M_i \begin{bmatrix} U_0 \\ u_0 \end{bmatrix}. \quad \text{(A4)}$$

Then we have

$$\begin{bmatrix} \bar{U} \\ \bar{u} \end{bmatrix} = \bar{M} \begin{bmatrix} U_0 \\ u_0 \end{bmatrix}, \qquad \begin{bmatrix} \delta U \\ \delta u \end{bmatrix} = \delta M \begin{bmatrix} U_0 \\ u_0 \end{bmatrix}, \quad \text{(A5)}$$

with

$$\bar{M} = \frac{M_i + M_j}{2}, \qquad \delta M = M_i - M_j. \quad \text{(A6)}$$

APPENDIX B: DERIVATION OF EQ. (47)

Recalling that G, g, and f are given as a quadratic form of $\bar{U}$, $\bar{u}$, U, and u, it is easy to show that Φ reduces to a simple form

$$\Phi(\bar{U}, \bar{u}, U, u) = A\bar{U}^2 + B\bar{u}^2 + C\bar{U}\bar{u} + D\bar{U} + E\bar{u} + F, \quad \text{(B1)}$$

where the coefficients $A - F$ are given as functions of U, u, and parameters that define the MBW configuration, such as μ, ν, $\hat{Z}$, and ψ. Then, the integration in Eq. (45) can be analytically done to give

$$W_{ij}(U, u) = W_0 \frac{2\psi}{\sqrt{4AB - C^2}} \times \exp\left(-\frac{BD^2 - CDE + AE^2}{4AB - C^2} + F \right). \quad \text{(B2)}$$

In principle, explicit forms of $A - F$ can be mathematically derived, however, such operations will be cumbersome, and even if successful, the resultant formulas can be potentially too complicated to be numerically implemented. Here, instead of such a rigorous analytical method, we present a more reasonable alternative to evaluate these coefficients by a simple numerical operation.

First, we prepare a numerical routine to compute $\Phi(\bar{U}, \bar{u}, U, u)$ based on Eq. (46), which is easily implemented once the transfer matrices at the subsection boundaries are defined. Next, at a given grid point (U, u), we evaluate Φ for six different combinations of $(\bar{U}, \bar{u})$ as follows

$$(\bar{U}, \bar{u}) = (0,0), (\pm 1, 0), (0, \pm 1), (1, 1). \quad \text{(B3)}$$

Then, introducing $\Phi_{\bar{U},\bar{u}} \equiv \Phi(\bar{U}, \bar{u}, U, u)$, the coefficients $A-F$ are given as

$$\begin{aligned} A &= \frac{\Phi_{1,0} + \Phi_{-1,0}}{2} - \Phi_{0,0}, \\ B &= \frac{\Phi_{0,1} + \Phi_{0,-1}}{2} - \Phi_{0,0}, \\ C &= \Phi_{0,0} + \Phi_{1,1} - \Phi_{1,0} - \Phi_{0,1}, \\ D &= \frac{\Phi_{1,0} - \Phi_{-1,0}}{2}, \\ E &= \frac{\Phi_{0,1} - \Phi_{0,-1}}{2}, \\ F &= \Phi_{0,0}, \end{aligned} \quad \text{(B4)}$$

with which W_{ij} is easily evaluated by Eq. (47).

APPENDIX C: COMPARISON USING SPRING-8-II PARAMETERS

The comparison made in Sec. IV between the MC simulation and FC method is based on the parameters in SPring-8, or the third generation SR facility. To examine the validity of the FC method in the fourth generation facility, a comparison is made using the parameters summarized in Table III, which are supposed in SPring-8-II [12]. The results are shown in Table IV in the same format as Table II. Note that the third harmonic radiation is chosen in this example so that the target photon energy is

TABLE III. Electron and undulator parameters supposed in SPring-8-II.

Electron energy	6 GeV
Beam current	200 mA
Natural emittance	6×10^{-11} m rad
Coupling constant	0.2
Energy spread	1.16×10^{-3}
Horizontal betatron function	4.6 m
Vertical betatron function	2.3 m
Undulator period	22 mm
Undulator K value	1.98
Fundamental photon energy	5.27 keV
Segment length (L_u)	2.6 m
Intersegment distance (L)	7.3 m
Matching section length (L_M)	2.8 m

TABLE IV. Comparison between the MC simulation and FC method using the parameters shown in this table.

Method	MC	FC	MC	FC
Energy spread	Without		With	
$\mathcal{B}_x$	2.35×10^{18}	2.46×10^{18}	1.96×10^{18}	2.00×10^{18}
ζ_x	7.24×10^{-2}	7.38×10^{-2}	5.79×10^{-2}	5.63×10^{-2}
τ_x (s)	665	1.8	1400	2.0
$\mathcal{B}_y$	8.99×10^{18}	9.16×10^{18}	6.13×10^{18}	6.32×10^{18}
ζ_y	0.195	0.197	0.139	0.141
τ_y (s)	280	1.9	460	6.5

the same as the former one (15.8 keV), because of the lower fundamental photon energy (5.27 keV).

We find a good agreement between the MC simulation and FC method in terms of the brilliance ($\mathcal{B}_{x,y}$) and degree of coherence ($\zeta_{x,y}$), and a significant reduction of the computation time ($\tau_{x,y}$), regardless of the large difference in the parameters.

[1] E. Wigner, On the quantum correction for thermodynamic equilibrium, Phys. Rev. **40**, 749 (1932).

[2] K.-J. Kim, A new formulation of synchrotron radiation optics using the Wigner distribution, *Insertion Devices for Synchrotron Sources*, edited by I. E. Lindau-R. O. Tatchyn (International Society for Optics and Photonics-SPIE, 1986). Vol. 0582, pp. 2–9, 10.1117/12.950906.

[3] R. Coisson and R. P. Walker, Phase space distribution of brilliance of undulator sources, *Insertion Devices for Synchrotron Sources*, edited by I. E. Lindau-R. O. Tatchyn (International Society for Optics and Photonics-SPIE, 1986). Vol. 0582, pp. 24–31, 10.1117/12.950909.

[4] K.-J. Kim, Characteristics of synchrotron radiation, AIP Conf. Proc. **184**, 565 (1989).

[5] J. Bahrdt, Wave-front propagation: Design code for synchrotron radiation beam lines, Appl. Opt. **36**, 4367 (1997).

[6] I. V. Bazarov, Synchrotron radiation representation in phase space, Phys. Rev. ST Accel. Beams **15**, 050703 (2012).

[7] T. Tanaka, Numerical methods for characterization of synchrotron radiation based on the Wigner function method, Phys. Rev. ST Accel. Beams **17**, 060702 (2014).

[8] T. Tanaka, Coherent mode decomposition using mixed Wigner functions of Hermite–Gaussian beams, Opt. Lett. **42**, 1576 (2017).

[9] A. Q. R. Baron, T. Tanaka, K. Soutome, M. Takao, T. Nakamura, K. Kobayashi, T. Fujita, S. Takahashi, H. Aoyagi, Y. Shimosaki, T. Seike, H. Uchiyama, D. Ishikawa, T.-H. Chuang, H. Kimura, H. Tanaka, H. Kitamura, and T. Ishikawa, Toward operation of series IDs at BL43LXU of SPring-8, AIP Conf. Proc. **1741**, 020033 (2016).

[10] A. Luis, Overall degree of coherence for vectorial electromagnetic fields and the wigner function, J. Opt. Soc. Am. A **24**, 2070 (2007).

[11] T. Tanaka, Major upgrade of the synchrotron radiation calculation code *SPECTRA*, J. Synchrotron. Radiat. **28**, 1267 (2021).

[12] H. Tanaka *et al.*, Green upgrading of SPring-8 to produce stable, ultrabrilliant hard X-ray beams, J. Synchrotron. Radiat. **31**, 1420 (2024).